EXPRESS LETTER

Three-dimensional shape distribution of lunar regolith particles collected by the Apollo and Luna programs

Akira Tsuchiyama[1,2,3]* , Takashi Sakurama[4], Tsukasa Nakano[5], Kentaro Uesugi[6], Makiko Ohtake[7], Takashi Matsushima[8], Kazuo Terakado[9] and Erik M. Galimov[10]

Abstract

The shapes of regolith particles on airless bodies, such as the Moon and asteroids, are important to understand their formation and evolution on surfaces. Limited studies have shown that the three-dimensional (3D) shapes of lunar regolith particles are, on average, more equant (spherical) than those of asteroid Itokawa or fragments by impact experiments. Therefore, more studies are required to determine whether such a feature is common. Accordingly, we performed X-ray microtomography imaging of lunar regolith particles collected by the Apollo program by NASA and the Luna program by the Soviet Union to obtain their 3D shapes. The ten samples (65 to 1108 particles/sample) examined had varieties of sampling sites (maria and highlands), reflecting the difference in materials (basalts and anorthosites, respectively, in general), regolith maturities, particle size ranges (< 74 to 450 μm), and petrographic textures (monomineralic, polymineralic, and agglutinate). The 3D particle shape distributions regarding three-axial length ratios ($L{:}I{:}S$, where L, I, and S are the longest, intermediate, and shortest lengths, respectively) showed that the average three-axial ratios were almost similar among the samples, irrespective of the sampling sites, maturities, and the size ranges [$S/I = 0.770(8)$, $I/L = 0.758(10)$, and $S/L = 0.581(11)$ for whole samples]. The 3D shapes of lunar particles were more equant (spherical) than those of the particles collected from asteroid Itokawa and fragments by hypervelocity impact experiments which had the average ratios similar to the 2D silver ratio ($S/I = I/L = 0.707$ and $S/L = 0.500$). These findings showed that the balance between impact fragmentation and mechanical abrasion controls the 3D shapes of lunar particles because impact and particle motion on the Moon's surface occur for a longer duration; however, impact fragmentation on this small asteroid surface primarily controls those of Itokawa particles. We also found shape dependence on petrographic textures of the lunar particles, and this could be explained by the strength of the materials against abrasion. The results obtained in this study will be the basic data to be compared with upcoming new results, such as particles collected from asteroid Ryugu, possibly from asteroid Bennu and Martian moons.

Keywords: X-ray tomography, Three-axial ratio, Airless body, Impact, Abrasion, Asteroid Itokawa

*Correspondence: atsuchi@fc.ritsumei.ac.jp

[1] Research Organization of Science and Technology, Ritsumeikan University, 1-1-1 Nojihigashi, Kusatsu 525-8577, Japan
Full list of author information is available at the end of the article

Graphical Abstract
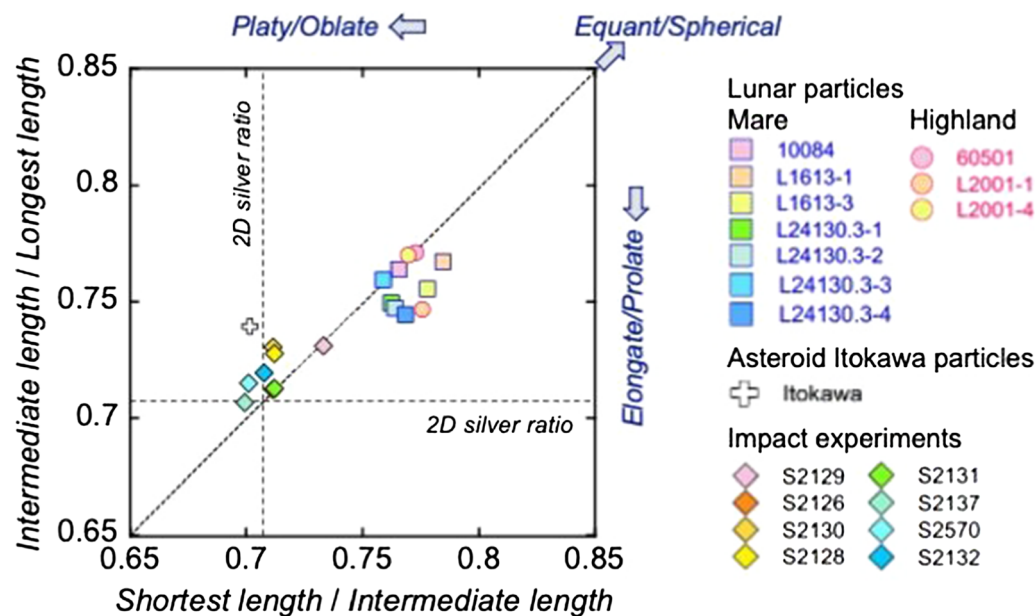
Main text

Introduction

Three-dimensional (3D) shapes of regolith particles are important for understanding their formation and evolution on airless bodies, such as Moon and asteroids (e.g., Tsuchiyama et al. 2011, 2014; Katagiri et al. 2014). The 3D shapes of asteroid Itokawa regolith particles were examined using microtomography (Tsuchiyama et al. 2011, 2014, 2017), and their shape distribution regarding the three-axial length ratio is comparable to that of fragments by hypervelocity impact experiments (Fujiwara et al. 1978; Capaccioni et al. 1984, 1986; Michikami et al. 2016, 2018), indicating that they were formed by impact (Tsuchiyama et al. 2011, 2014, 2017; Michikami et al. 2018). The rounded edges observed on some Itokawa particles suggest that mechanical abrasion and impact fragmentation have occurred (Tsuchiyama et al. 2011, 2014; Matsumoto et al. 2016).

The 3D particle shape also provides important information on the mechanical properties of regolith. Because shapes substantially affect the regolith's strength, angle of repose, packing density, and ability of regolith particles to be attached to and abrade spacecraft materials or clog air filters, the 3D shapes of lunar regolith particles have been studied for samples collected by the Apollo and Luna programs (e.g., Liu et al. 2008; Katagiri et al. 2014) and their analogs (Matsushima et al. 2009). Katagiri et al. (2014) proposed from the 3D shapes measured by X-ray

microtomography that lunar particles collected from Descartes Highlands (Apollo 16 sample 60501) are, on average, more equant (spherical) than Itokawa particles. However, locality (mare or highland), regolith maturity, which is the degree (regarding residence time) of evolution by space weathering, impact and grain motion on the lunar surface, particle size, and petrographic texture all contribute to the diversity of lunar regolith. Notably, the only reliable data came from Katagiri et al. (2014), who used a small number of particles ($N=74$) and a limited size range (105–250 μm). The available data are insufficient to discuss the formation and evolution of the lunar regolith. Therefore, in this study we measured the 3D shapes for samples with different size ranges, various localities by the Apollo and Luna missions, and maturities by performing X-ray microtomography imaging of a large number of particles for each sample at a time, after which differences in particle size, sampling sites, and maturities were verified. The difference between petrographic textures was also examined. To understand the formation and evolution of lunar regolith particles, the results were compared with previous studies on Itokawa particles (Tsuchiyama et al. 2014, 2017) and hypervelocity impact experiments (Michikami et al. 2018).

The present study is also important as the basic data to be compared with upcoming new results for particles that were returned from asteroid Ryugu by the Hayabusa2 mission (e.g., Tachibana et al. 2022; Nakamura

Tsuchiyama *et al. Earth, Planets and Space*   (2022) 74:172

Page 3 of 11

et al. 2022) and will be returned from asteroid Bennu by the Origins, Spectral Interpretation, Resource Identification, Security, Regolith Explorer (OSIRIS-REx) mission (e.g., Lauretta et al. 2019), and Martian moons by the Martian Moons eXploration (MMX) mission (e.g., Usui et al. 2020).

Experiments

Table 1 lists the study samples retrieved from the Moon. The samples in Apollo 11, Luna 16, and Luna 24 missions were lunar maria soils, whereas those in Apollo 16 and Luna 20 missions were lunar highland soils. These samples were sieved into different fractions. The ratio of ferromagnetic resonance intensity (Is) to the total Fe content (expressed as FeO, written as Is/FeO) is a good measure of maturity of a lunar soil (Heiken et al. 1991). Among the samples examined, Is/FeO was only measured for the Apollo samples: 78 and 80 for Apollo 11 (10,084) and Apollo 16 (60,501) samples, respectively, indicating that they are matured (Morris 1978). The Luna 16 sample (L1613) has the mean grain size of 85 μm and the sorting of −2.07φ (Stakheev 1979), which correspond to mature and submature, respectively (Heiken et al. 1991). The Luna 20 sample (L2001) has the mean grain size of 77 μm and the sorting of −2.71 φ (Stakheev 1979), which correspond to mature and submature, respectively (Heiken et al. 1991). The Luna 24 sample (L24130) has the agglutinate content of 14% (Rode et al. 1980), which corresponds to immature (Heiken et al. 1991). A sample (L24149), which is stratigraphically closest to L24130, has Is/FeO of 21 (Morris 1977), corresponding to immature as well.

X-ray microtomography was used to image a large number of particles, *N*, ranging from 65 to 1108 in each sample, at beamline BL20B2 of SPring-8, Japan's synchrotron radiation facility. Particles, which were randomly selected from each sample, were placed on a double-stick tape looped around a wooden toothpick or an aluminum rod of 2.3 mm or 2.6 mm in diameter, respectively, and ∼4–10 mm in length (Additional file 2Fig. S1A). A set of 1800 projection images (every 0.01 deg in 180 deg) was taken at the X-ray energy of 18, 20, and 25 keV (Table 1). Then, a series of absorption CT images (2048 × 2048 in matrix) with the voxel sizes of 1.30, 1.73, or 1.74 μm/voxel (effective spatial resolution: 4–5 μm) (e.g., Additional file 2: Fig. S1B) were reconstructed using a filtered back projection algorithm (Nakano et al. 2000) for obtaining 3D images. Two or three sets of imaging were obtained for each sample (e.g., U, M, and L in Additional file 2: Fig. S1A) by moving the sample along the rod direction to cover a whole sample area with overlapping.

Image analysis was performed using a software package of SLICE (Nakano et al. 2006) and ImageJ. The protocol is

as follows: (1) combining two or three sets of CT images into a series of 3D images for each sample, (2) extraction of particles by binarization using a threshold determined manually in CT images, (3) recognition of individual particles by removing multiple particles sticking together if necessary, (4) removing small particles that give large errors in three-axial ratios (the number of voxels of < 10,000), and (5) obtaining the three-axial lengths of each particle using a bounding box method (Michikami et al. 2018) with the longest, intermediate, and shortest lengths ($L \geq I \geq S$), which were determined in the order of *S*, *I*, and *L*, respectively (method BU in Michikami et al. 2018). Ellipsoid approximation (Ikeda et al. 2000) was also used to obtain the longest, intermediate, and shortest lengths ($a \geq b \geq c$) for comparison with some previous studies. Each particle was classified into three categories based on the petrographic texture in CT images as follows: monomineralic (m-type), primarily comprising a single mineral grain (olivine, pyroxene, or plagioclase) (Fig. 1A); polymineralic (p-type), mainly comprising multi-mineral phases (groundmass in basalts or breccia) (Fig. 1B); and agglutinate (ag-type), mostly comprising vesiculated material by partial melting (Fig. 1C). Some vesiculated materials, more or less, adhere to many m- and p-type particles. If the amounts of vesiculated material and m- and p-type material are similar, we refer to them as ag/m-type and ag/p-type, respectively. Glassy spherules were also present but excluded from the present analysis.

Results

Additional file 1: Table S1 lists the average three-axial ratios obtained by bounding box and ellipsoid approximation for each lunar sample with textural types, along with the intermediate length, *I*, as the representative of the particle size. Each histogram of *I* for the sample has a simple shape with a single peak except for two samples of relatively large grains (L24130.3–4 and L2001-4), where a second peak clearly separated from the main peak was present. The maximum particle size (*I*) of each sample was similar or slightly exceeded the largest sieve opening size (Additional file 1: Table S1). In contrast, the second peaks in L24130.3–4 and L2001-4 (at ∼75 and ∼ ∼90 μm, respectively) were smaller than that of the main peak and also smaller than the smallest sieve opening size, suggesting that these grains should be fragmented after sieving. Therefore, the grains belonging to these second peaks were excluded from the present analysis. Thus, a number of particles analyzed were reduced from 102 to 70 for L24130.3–4 and from 103 to 77 for L2001-4. The particle size (median, minimum, or maximum) was similar among different textural types (m-, p-, and ag-types) for
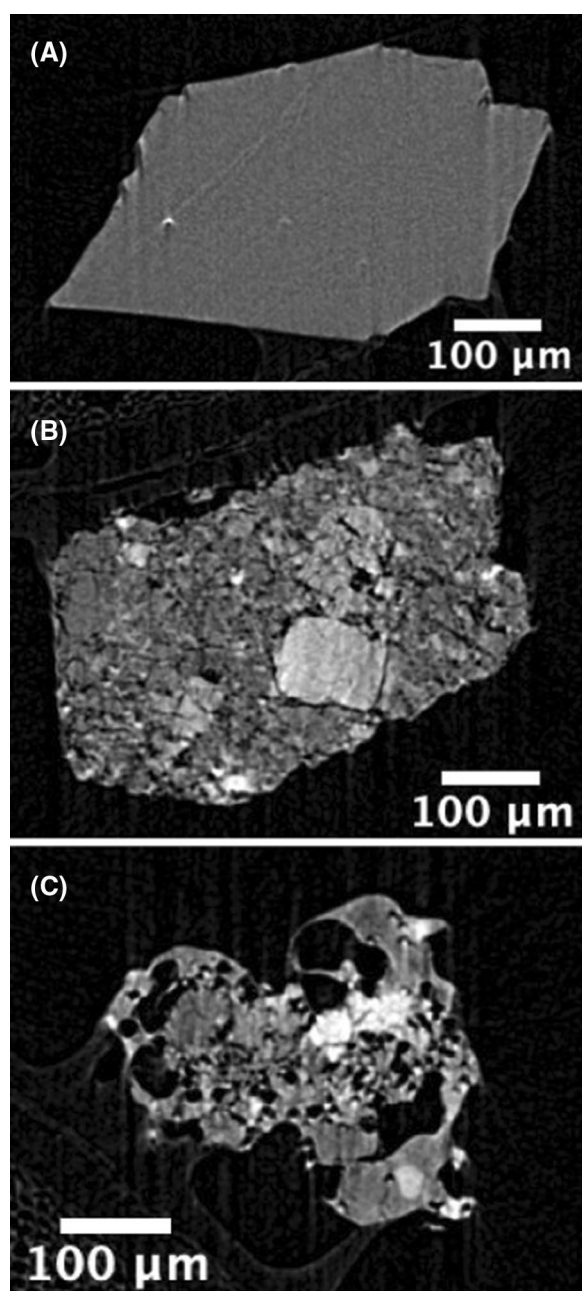
Tsuchiyama *et al. Earth, Planets and Space*   (2022) 74:172

Page 4 of 11

Fig. 1 Typical CT images of lunar regolith particles. **A** Monomineralic (m-type) particle. **B** Polymineralic (p-type) particle. **C** Agglutinate (ag-type) particle. Luna24 sample L2001-4

samples of a large number of particles (N) (L24130.3–2, L1613-1, and L24130.3–3) (Additional file 1: Table S1), indicating no significant size difference among particles of different textures.

Figure 2 shows typical results of the 3D shape distributions of particles as Zingg diagrams, where I/L is plotted against S/I. In this diagram, a sphere is plotted at $I/L = S/I = 1$, whereas plate-like (oblate) and rod-like (prolate) objects are plotted in the upper left ($I/L > S/I$) and lower right ($I/L < S/I$) regions, respectively. Figure 2 also shows the 2D silver ratio ($I/L = S/I = 1/\sqrt{2} \sim 0.707$) that corresponds to the average of the three-axial ratio of fragments produced by impact experiments (Michikami et al. 2016, 2018). The aspect ratio defined by S/L increased from the lower left to the upper right of this diagram.

Many particles were distributed in a region larger than the silver ratio (Fig. 2), but they seemed to be almost equally distributed in the oblate and prolate fields irrespective of the textural types. However, if we plot the averages of individual textural types (Additional file 2: Fig. S2), ag-types and some of m- and p-types are in the prolate field, while m-type of L2001-4 and p-type of 10,084 are in the oblate field. The deviation from the $I/L = S/I$ line for some samples may be caused from a limited numbers of particles measured (e.g., $N = 12$ for m-type of L2001-4). Notably, the average aspect ratio (S/L) of ag-type particles may exceed that of p-type particles, which may also exceed that of p-type particles (Additional file 2: Fig. S2). This was clear for the sample of the largest N (L24130.3–2 in Fig. 2B). To quantitatively check this possibility, we performed Kolmogorov–Smirnov (K–S) tests on the shape distributions among the three sets of the two textural-type combinations (m *vs.* p, m *vs.* ag, and p *vs.* ag) for each sample. The values of the three sets of the probability in the K–S test, P, were 0.00 in the sample of largest N (L24130.3–2), indicating that the shape distributions are distinguishable among m, p, and ag, whereas the P-values exceeded a threshold (0.05) for most of the other samples, suggesting that the shape distribution is not distinguishable except for m *vs.* p and p *vs.* ag in 10,084 and m *vs.* p in L24130.3–3 (Table 2). This may suggest that the ag-type particles are more equant than the p-type particles, which are more equant than the m-type particles on average.

Figure 3A depicts the average three-axial ratio of whole particles, including whole texture types (m-, p-, ag-, ag/m-, and ag/p-types) for each sample. They roughly aligned along the $I/L = S/I$ line, although many of them were plotted slightly toward the lower right side (prolate side), suggesting that the particles in some samples tended to be slightly prolate on average. The aspect ratio (S/L) ranged from 0.570 (L24130.3–4) to 0.601 (L1613-1) and the average three-axial ratios of the whole sample were $S/I = 0.770(8)$, $I/L = 0.758(10)$, and $S/L = 0.581(11)$ (Additional file 1 Table S1). The K–S tests on the shape showed that the P-values between the two samples of the whole sample combination exceeded 0.05, showing that the shape distributions were not distinguished except for the set between 60,501 *vs.* L24130.3–2 (Table 2).

Tsuchiyama *et al. Earth, Planets and Space*   (2022) 74:172
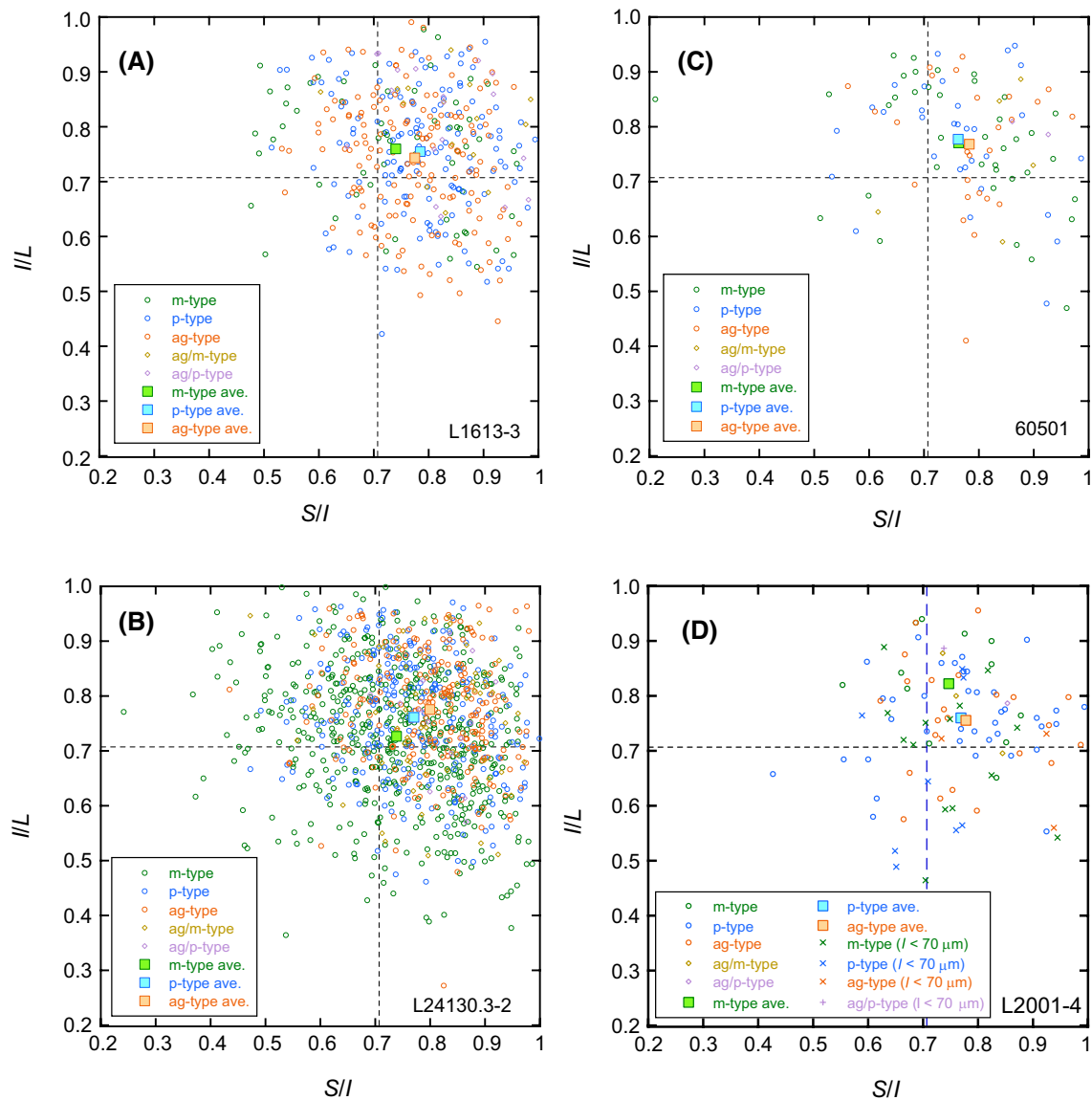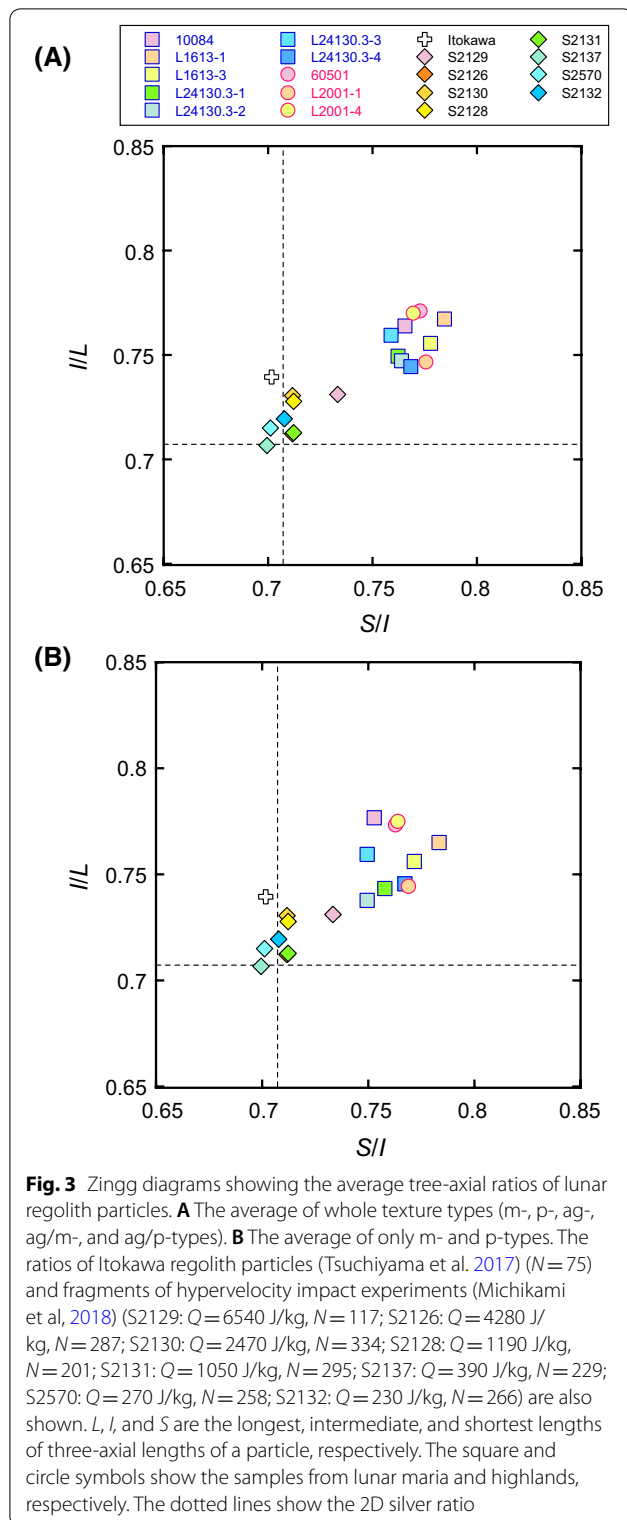
Page 5 of 11

Fig. 2 Zingg diagrams of lunar regolith particles showing typical particle shape distributions. **A** L1613-3 from Mare Fecunditatis (127–200 μm, mature or submature, and *N* = 389). **B** L24130.3–2 from Mare Crisium (74–95 μm, immature, and *N* = 1108). **C** 60,501 from Descartes Highland (75–105 μm, mature, and *N* = 104). **D** L2001-4 from Apollonius Highlands (200–450 μm, mature or sub mature, and *N* = 77). × and + denote particles in the second peak of the particle size histogram (*l* < 70 μm). *L*, *l*, and *S* are the longest, intermediate, and shortest lengths of three-axial lengths of a particle, respectively. The dotted lines show the 2D silver ratio

Because the three-axial ratios of ag-type particles might be affected by their original molten shapes, the three-axial ratios of only m- and p-type particles were also examined. Figure 3B shows the average three-axial ratios of these particles. The aspect ratio (*S/L*) ranged from 0.550 (L24130.3–2) to 0.598 (L1613-1) (Fig. 3A), and the average three-axial ratios of the whole sample were $S/I = 0.763(11)$, $I/L = 0.758(15)$, and $S/L = 0.575(10)$ (Additional file 1: Table S1). These results showed that

the samples of m- and p-types were slightly less equant than those of the whole texture types. The K–S tests on the shape for m- and p-types also showed that the *P*-values between the two samples mostly exceeded 0.05, showing that the shape distributions were not distinguished except for four sets (Table 2).

Tsuchiyama *et al. Earth, Planets and Space* (2022) 74:172

Page 6 of 11

Fig. 3 Zingg diagrams showing the average tree-axial ratios of lunar regolith particles. **A** The average of whole texture types (m-, p-, ag-, ag/m-, and ag/p-types). **B** The average of only m- and p-types. The ratios of Itokawa regolith particles (Tsuchiyama et al. 2017) ($N=75$) and fragments of hypervelocity impact experiments (Michikami et al, 2018) (S2129: $Q=6540$ J/kg, $N=117$; S2126: $Q=4280$ J/kg, $N=287$; S2130: $Q=2470$ J/kg, $N=334$; S2128: $Q=1190$ J/kg, $N=201$; S2131: $Q=1050$ J/kg, $N=295$; S2137: $Q=390$ J/kg, $N=229$; S2570: $Q=270$ J/kg, $N=258$; S2132: $Q=230$ J/kg, $N=266$) are also shown. *L*, *I*, and *S* are the longest, intermediate, and shortest lengths of three-axial lengths of a particle, respectively. The square and circle symbols show the samples from lunar maria and highlands, respectively. The dotted lines show the 2D silver ratio

Discussion
3D shape distribution among lunar particles
The 3D shape distributions of the lunar regolith particles (Fig. 3) and K–S tests (Table 2) showed that their shape features were almost similar among the samples examined in this study, not only for the samples of the whole texture types but also for the samples of m- and p-types, irrespective of their particle size fractions (from < 74 μm to 200–450 μm), locality (mare and highlands), and regolith maturity. The average three-axial ratios of the whole sample markedly exceeded the 2D silver ratios ($S/I=I/L=0.707$ and $S/L=0.500$). So far, only a limited number of the three-axial ratios of lunar regolith particles have been measured. Heywood (1971) measured the Apollo 12 sample 12,057.72 ($N=30$; ~ 700 μm) of $S/I=0.730$–0.855 and $I/L=0.725$–0.758. Mahmood et al. (1974) reported the I/L of the weighted averages of Apollo 14 and 15 samples ($N=1136$; 44–2300 μm); one of the values (0.763 for 14,259.3) is clearly more equant than the 2D silver ratios and two of them (0.725 for 14,163.148 and 0.719 for 15,601.82) are larger than the value of the 2D silver ratios, although the data may be inaccurate compared to the X-ray tomography data. Katagiri et al. (2014) measured the 3D shape distribution of the Apollo 16 sample 60,501 ($N=74$; 105–250 μm) using X-ray microtomography and showed that the averaged ratios were $c/b=0.764$, $b/a=0.777$, and $c/a=0.593$, where the three-axial ratios ($a\geq b\geq c$) were obtained by ellipsoid approximation. The particle size range of 60,501 measured in the present study (75–105 μm) was smaller than that of the previous study. The average three-axial ratio in the present study by ellipsoid approximation ($c/b=0.744$, $b/a=0.742$, and $c/a=0.551$) was less equant than Katagiri's data. However, the K–S test between the two datasets gave $P=0.20$, indicating that the 3D shape distributions are not distinguishable. Therefore, the present data are consistent with previous studies.

Comparison with Itokawa particles
Regolith particles of S-type asteroid Itokawa, which corresponds to LL4 ~ 6 ordinary equilibrated chondrites, were collected by JAXA's Hayabusa mission and their 3D shape distribution ($N=47$; 13–114 μm) was measured by Tsuchiyama et al. (2014). The average three-axial ratios were $c/b=0.61$, $b/a=0.72$, and $c/a=0.44$ by ellipsoid approximation, which were smaller than the average ratio of the whole lunar regolith particles by ellipsoid approximation in the present study ($c/b=0.738(8)$, $b/a=0.732(8)$, and $c/a=0.538(8)$). An additional measurement of totally 75 particles by Tsuchiyama et al. (2017) showed that $S/I=0.702$, $I/L=0.740$, and $S/L=0.514$, which were clearly smaller than those of the whole lunar particles both for the whole texture types (Fig. 3A) and m- and p-types (Fig. 3B). The K–S tests showed that the distributions of lunar regolith particles and Itokawa particles are distinguishable ($P=0.00$–0.05), except for the two samples for the whole texture types ($P=0.10$

Tsuchiyama *et al. Earth, Planets and Space*   (2022) 74:172

Page 7 of 11

Table 1 Lunar regolith samples imaged by microtomography in the present study

Sample	Mission	Sampling site	Grain size (µm)	Maturity	Energy (kev)	Voxel size (µm)	N
10084	Apollo 11	Mare Tranquillitatis	75–105	Mature[2]	20. 24.9	1.73, 1.74	199
L1613-1	Luna 16	Mare Fecunditatis	<83	Mature or submature	25	1.3	107
L1613-3			127–200		20, 24.9	1.73, 1.74	389
L24130.3-1	Luna 24	Mare Crisium	<74	Immature	25	1.3	65
L24130.3-2			74–95		20, 24.9	1.73, 1.74	1108
L24130.3-3			95–200		20, 24.9	1.73, 1.74	318
L24130.3-4			200–370		20	1.73	70 (102)[4]
60501[1]	Apollo 16	Descartes highlands	75–105	Mature[3]	20	1.73	104
L2001-1	Luna 20	Apollonius highlands	<83	Mature or submature	25	1.3	143
L2001-4			200–450		17.9, 18.1, 24	1.73, 1.74	77 (103)[4]

[1] Particles of 105–250 µm in size also examined with microtomography by Katagiri et al. (2014)

[2] Is/FeO = 78 (Morris et al. 1978)

[3] Is/FeO = 80 (Morris et al. 1978)

[4] Small particles that might be formed by fragmentation after sieving were omitted in the analysis (the total number of the particles measured are shown in the parenthesis)

and 0.07 for Itokawa *vs.* L24130.3–1 and L24130.3–4, respectively) and the three samples for m- and p- types ($P = 0.16$, 0.10 and 0.05 for Itokawa *vs.* L24130.3-, L24130.3–2, and L24130.3–3, respectively) (Table 2).

Comparison with hypervelocity impact experiments
Michikami et al. (2018) performed hypervelocity impact experiments on basalt targets and measured the three-axial lengths of impact fragments by X-ray microtomography (8 runs; impact velocity from 1.60 to 7.13 km/s, specific density defined as the kinetic energy of the projectile per unit target mass, Q, from 230 to 8540 J/kg, which corresponds to impact conditions for catastrophic destruction to cratering). The three-axial ratios of small impact fragments (<120 µm), which were comparable to the sizes of Itokawa and most of the lunar particles, were similar among the 8 runs, regardless of the Q values, and similar to the 2D silver ratio (Fig. 3). These ratios were also similar to those of Itokawa regolith particles by Tsuchiyama et al. (2017). The K–S tests suggested that the shape distributions were not distinguishable among the runs and runs *vs.* Itokawa particles. Michikami et al. (2018) also examined the effect of petrographic texture and found that texture did not significantly affect the shape of fine fragments. In contrast, the petrographic texture influenced the shapes of fragments produced by thermal fatigue due to repeated day-and-night heating-and-cooling cycles should be influenced by the petrographic texture (Molaro et al. 2015). This strongly suggests that the Itokawa particles are not the products of thermal fatigue but impact fragments on the asteroid surface. If we compare the average three-axial ratios, the lunar regolith particles are more equant than the impact

fragments on average both for the whole texture types (Fig. 3A) and m- and p-types (Fig. 3B). The K–S test showed that the distributions of lunar regolith particles and the impact fragments were distinguishable, except for the three sample sets for the whole texture types and the four sample sets for m- and p-types (Table 2), suggesting that the lunar regolith particles with variable locality and maturity were more equant (spherical) than the fragments of the hypervelocity impact experiments.

The following processes impart equant shapes to lunar regolith particles during their long residence time on the surface: (1) mechanical abrasion by particle motion during impact gardening (Tsuchiyama et al. 2011, 2014), (2) repeated fragmentation of regolith particles by repeated impacts, (3) melting during impact, (4) thermal fatigue (Delbo et al. 2014), and (5) sputtering by the solar wind. Case 1 is possible because mechanical abrasion occurs even on the Itokawa surface of a much smaller size for a much shorter duration than on the lunar surface (Tsuchiyama et al. 2011, 2014). In Case 2, particles may become equant by multiple impacts although the average axial ratio of the fragments by a single impact should be close to the 2D silver ratio (2: $\sqrt{2}$: 1; $S/I = I/L = 0.707$ and $S/L = 0.500$), as already discussed (Michikami et al. 2018). However, considering the fractal nature of the 2D silver ratio, where homothetic rectangles are repeatedly formed by folding a rectangle with this ratio into halves, the average axial ratio of particles formed by repeated impacts might be maintained around the 2D silver ratio. The shape of multiple impacted particles might have a 3D silver ratio ($2^{2/3}$: $2^{1/3}$: 1; $S/I = I/L = 0.794$ and $S/L = 0.630$), where homothetic cuboids are repeatedly formed by breaking a cuboid with this ratio into halves, instead of

Tsuchiyama *et al. Earth, Planets and Space*   (2022) 74:172

Page 8 of 11

Table 2 Probabilities of Kolmogorov–Smirnov test for particle shape distributions among textural types and lunar vs. Itokawa and impact experiment samples

Texture *vs.* texture	10084	L1613-1	L1613-3	L24130.3-1	L24130.3-2	L24130.3-3	L24130.3-4	60501	L2001-1	L2001-4
m *vs.* p [1]	**0.02**	0.27	0.11	0.57	**0.00**	**0.03**	0.29	0.27	0.76	0.11
m *vs.* ag	0.21	0.25	0.15	0.13	**0.00**	0.10	0.13	0.26	0.22	0.13
p *vs.* ag	**0.00**	0.96	0.29	0.21	**0.00**	0.13	0.11	0.37	0.18	0.30
Whole particles										
Sample *vs.* sample	10084	L1613-1	L1613-3	L24130.3-1	L24130.3-2	L24130.3-3	L24130.3-4	60501	L2001-1	L2001-4
N	199	107	389	65	1108	318	70	104	143	77
L1613-1	0.29	–	–	–	–	–	–	–	–	–
L1613-3	0.33	0.66	–	–	–	–	–	–	–	–
L24130.3-1	0.49	0.29	0.54	–	–	–	–	–	–	–
L24130.3-2	0.36	0.11	0.25	0.67	–	–	–	–	–	–
L24130.3-3	0.30	0.22	0.32	0.68	0.30	–	–	–	–	–
L24130.3-4	0.55	0.50	0.67	0.89	0.72	0.77	–	–	–	–
60501	0.15	0.73	0.20	0.12	**0.03**	0.19	0.40	–	–	–
L2001-1	0.06	0.07	0.11	0.40	0.16	0.10	0.37	0.10	–	–
L2001-4	0.17	0.60	0.25	0.27	0.07	0.21	0.24	0.33	0.09	–
Itokawa [2]	**0.01**	**0.00**	**0.00**	0.10	**0.01**	**0.01**	0.07	**0.00**	**0.05**	**0.00**
S2129 [3]	**0.02**	**0.00**	**0.00**	0.16	**0.01**	**0.01**	0.10	**0.00**	**0.01**	**0.00**
S2126 [3]	**0.00**	**0.00**	**0.00**	**0.03**	**0.00**	**0.00**	**0.00**	**0.00**	**0.00**	**0.00**
S2130 [3]	**0.00**	**0.00**	**0.00**	0.05	**0.00**	**0.00**	**0.02**	**0.00**	**0.00**	**0.00**
S2128 [3]	**0.00**	**0.00**	**0.00**	**0.05**	**0.00**	**0.00**	**0.02**	**0.00**	**0.01**	**0.00**
S2131 [3]	**0.00**	**0.00**	**0.00**	**0.01**	**0.00**	**0.00**	**0.00**	**0.00**	**0.00**	**0.00**
S2137 [3]	**0.00**	**0.00**	**0.00**	**0.01**	**0.00**	**0.00**	**0.01**	**0.00**	**0.00**	**0.00**
S2570 [3]	**0.00**	**0.00**	**0.00**	**0.01**	**0.00**	**0.00**	**0.00**	**0.00**	**0.00**	**0.00**
S2132 [3]	**0.00**	**0.00**	**0.00**	**0.00**	**0.00**	**0.00**	**0.00**	**0.00**	**0.00**	**0.00**
Monomineralic and polymineralic particles										
Sample *vs.* sample	10084	L1613-1	L1613-3	L24130.3-1	L24130.3-2	L24130.3-3	L24130.3-4	60501	L2001-1	L2001-4
N	117	83	202	62	796	258	61	70	119	50
L1613-1	0.27									
L1613-3	0.24	0.79								
L24130.3-1	0.32	0.27	0.43							
L24130.3-2	**0.02**	0.07	**0.02**	0.63						
L24130.3-3	0.15	0.33	0.25	0.60	0.21					
L24130.3-4	0.37	0.40	0.49	0.68	0.36	0.60				
60501	0.58	0.50	0.33	0.14	**0.04**	0.11	0.46			
L2001-1	0.11	0.10	0.08	0.63	0.15	0.12	0.37	0.12		
L2001-4	0.26	0.42	0.33	0.14	**0.02**	0.16	0.20	0.84	0.05	
Itokawa	**0.04**	**0.02**	**0.01**	0.16	0.10	0.05	**0.04**	**0.02**	0.08	**0.00**
S2129	**0.04**	**0.02**	**0.00**	0.25	0.09	**0.05**	**0.05**	**0.01**	**0.04**	**0.00**
S2126	**0.00**	**0.00**	**0.00**	0.06	**0.00**	**0.00**	**0.00**	**0.00**	**0.00**	**0.00**
S2130	**0.00**	**0.00**	**0.00**	0.09	**0.00**	**0.00**	**0.02**	**0.00**	**0.01**	**0.00**
S2128	**0.01**	**0.00**	**0.00**	0.08	**0.01**	**0.01**	**0.02**	**0.00**	**0.03**	**0.00**
S2131	**0.00**	**0.00**	**0.00**	**0.02**	**0.00**	**0.00**	**0.00**	**0.00**	**0.01**	**0.00**
S2137	**0.00**	**0.00**	**0.00**	**0.02**	**0.00**	**0.00**	**0.01**	**0.00**	**0.00**	**0.00**
S2570	**0.00**	**0.00**	**0.00**	**0.01**	**0.00**	**0.00**	**0.00**	**0.00**	**0.00**	**0.00**
S2132	**0.00**	**0.00**	**0.00**	**0.01**	**0.00**	**0.00**	**0.00**	**0.00**	**0.00**	**0.00**

[1] Textural types: m: monomineralic, p: polymineralic, ag: agglutinate

[2] Tsuchiyama et al. (2017)

[3] Impact experiments (Michikami et al. 2018): fine fragments (<120 μm)

S2129: Q = 8540 J/kg, N = 117; S2126: Q = 4280 J/kg, N = 287; S2130: Q = 2470 J/kg, N = 334; S2128: Q = 1190 J/kg, N = 201

S2131: Q = 1050 J/kg, N = 295; S2137: Q = 390 J/kg, N = 229; S2570: Q = 270 J/kg, N = 258; S2132: Q = 230 J/kg, N = 266

*The bold texts showing the probability, P, of <0.05, where two distributions are distinguishable

Tsuchiyama *et al. Earth, Planets and Space*   (2022) 74:172

Page 9 of 11

the 2D silver ratio, although we lack experimental evidence for this. If this is the case, the average axial ratio should be closer to the 3D silver ratio, but the present lunar samples lacked such large axial ratios. For Case 3, particles easily become rounded by melting. Actually, the ag-type particles seemed to be slightly more equant than the m- and p-type particles (Additional file 2: Fig. S2). However, as m- and p-type particles are also more equant than the 2D silver ratio, melting cannot explain the equant shapes of whole lunar regolith particles. In addition, many ag-type particles are fragments of larger agglutinate grains (Fig. 1C), at least in the present particle size range. As already mentioned, glassy spherules were excluded from the present study. In Case 4, the shapes of fragments formed by thermal fatigue should be mainly influenced by pre-existing cracks in larger grains and/or rocks based on the thermal fatigue experiments by Delbo et al. (2014). Although we do not know the 3D shapes of blocks surrounded by such cracks, we may expect a 2D silver ratio in this case if we assume the fractal nature of cracking. In Case 5, particle surfaces can be rounded by the sputtering. The width of amorphous rims on lunar regolith particle surfaces by space weathering is smaller than 1 μm (Pieters and Noble 2016). The amorphous layers were caused mainly by vaporization and redeposition due to micrometeorite bombardments and solar wind implantation. Sputtering by solar wind may cause rounded edges, but its contribution should not be large. Thus, sputtering may not the cause for a large change in the axial ratio.

Based on the above discussion, mechanical abrasion is the major process imparting equant shapes to lunar regolith particles, as in Case 1 where particles are more equant and spherical than impact fragments. Rounded surfaces formed by mechanical abrasion were observed on Itokawa particles by X-ray microtomography (Tsuchiyama et al. 2011) and scanning electron microscopy (SEM) (Matsumoto et al. 2016). In the SEM images of lunar samples, some particles were angular (Additional file 2: Fig. S3A) and had sharp edges and cleavage steps on the surfaces, which were formed by impact fragmentation (Additional file 2: Fig. S3B), whereas some were rounded with rounded edges formed by mechanical abrasion (Additional file 2: Fig. S3C), and no sharp edges, including cleavage steps, were seen on relatively smooth surfaces (Additional file 2: Fig. S3D). The strength of the materials against abrasion could explain why the p-type particles were slightly more equant than the m-type particles on average (e.g., Additional file 2: Fig. S2, Table 2); mineral grains (m-type) should be stronger than that of groundmass or brecciated grains (p-type) against abrasion. In contrast, the petrographic texture of the target

basalt (phenocryst and groundmass rich) did not significantly affect the shape of fine fragments of the impact experiments (Michikami et al. 2018). Ag-type particles might be more easily abraded because they have many small bubbles (Fig. 1C). The shape of ag-type particles might be affected by melting but CT images showed that many ag-type particles were fragments of larger agglutinate grains. Thus, m-, p-, and ag-type particles of similar to the silver ratio on the averages formed first by impact and became equant in sequence by mechanical abrasion.

The effect of impact on the lunar surface is much larger than that on Itokawa, even with a single impact event, owing to the larger energetic scale of impact on the Moon. As this provides intense mechanical abrasion by impact-induced particle motion, the regolith particles become spherical from fragmented particles. As abrasion proceeds, the particle shape becomes a sphere in extreme cases. The regolith particles are also fragmented by impact. Thus, the average three-axial ratios of actual regolith particles should be between 1:1:1 (sphere) and 2:$\sqrt{2}$:1 (2D silver ratio). The similar average ratios of the lunar regolith particles, regardless of maturity, suggests that the average axial ratio became saturated by the trade-off between mechanical abrasion and impact fragmentation. The time scale for this saturation may not be long because the 3D shape distributions of the immature samples (L23130.3–1 ~ L23130.3–4) were not distinguishable from the other mature or submature samples except for L23130.3–2 vs. 60501 (Table 2). It should be noted that the average three-axial lengths of the immature samples were slightly smaller than those of the other samples, suggesting incomplete saturation of the immature samples. In contrast, since the mechanical abrasion was very limited on Itokawa, we could not detect any clear change in the three-axial ratio of the Itokawa particles (Fig. 3), although rounded edges were observed.

Abbreviations

Supplementary Information

Tsuchiyama *et al. Earth, Planets and Space*   (2022) 74:172

Page 10 of 11

Author contributions
AT contributed to the design of the study, collection, analysis, and interpretation of data and writing the manuscript. TS contributed mainly to analysis, and interpretation of data and partly to writing the manuscript, KU mainly to collection of data, TN mainly to collection and interpretation of data, and MO, TM, KT, and EMG mainly to preparations of samples and interpretation of data. All the authors read and approved the final manuscript.

Authors' information
TN retired from The Institute of Geology and Geoinformation, AIST in March 2020 and is working for Geological Survey of Japan, AIST as a temporary staff at present.
TS graduated from Graduate School of Science, Kyoto University in March 2017 and is working as a civil service employee at present.
EMG died in October 2021.

Availability of data and materials
Data on the number of particles, the average three-axial ratios by bounding box and ellipsoid approximation and the mean, minimum, and maximum of intermediate lengths by bounding box for different samples with different textural types are available in additional file as Additional file 1: Table S1. The CT images of the samples are available if requested.

Declarations

Ethics approval and consent to participate
Not applicable.

Consent for publication
Not applicable.

Competing interests
The authors declare no competing interests.

Author details
[1]Research Organization of Science and Technology, Ritsumeikan University, 1-1-1 Nojihigashi, Kusatsu 525-8577, Japan. [2]CAS Key Laboratory of Mineralogy and Metallogeny/Guangdong Provincial Key Laboratory of Mineral Physics and Materials, Guangzhou Institute of Geochemistry, Chinese Academy of Sciences (CAS), Guangzhou 510640, People's Republic of China. [3]CAS Center for Excellence in Deep Earth Science, Guangzhou 510640, People's Republic of China. [4]Division of Earth and Planetary Sciences, Graduate School of Science, Kyoto University, Kitashirakawa-Oiwakecho, Sakyo-Ku, Kyoto 606-8502, Japan. [5]The Institute of Geology and Geoinformation, National Institute of Advanced Industrial Science and Technology (AIST), Tsukuba Central 7, 1-1-1 Higashi, Tsukuba, Ibaraki 305-8567, Japan. [6]The Scattering and Imaging Division, Japan Synchrotron Radiation Research Institute (JASRI), 1-1-1Sayo-Cho, Sayo-Gun, Kouto, Hyogo 679-5198, Japan. [7]Department of Computer Science and Engineering/Division of Information Systems, The University of Aizu, Aizu-Wakamatsu, Fukushima Pref 965-8580, Japan. [8]Institute of Systems and Information Engineering, University of Tsukuba, Tennodai 1-1-1, Tsukuba 305-8573, Japan. [9]Japan Space Forum, 3-2-1, Kandasurugadai, Chiyoda-Ku, Tokyo 101-0062, Japan. [10]V.I. Vernadsky Institute of Geochemistry and Analytical Chemistry, Kosygina Str.19, Moscow 119991, Russian Federation.

References
Capaccioni F, Cerroni P, Coradini M, Farinella P, Flamini E, Martelli G, Paolicchi P, Smith PN, Zappa V (1984) Shapes of asteroids compared with fragments from hypervelocity impact experiments. Nature 308:832–834. https://doi.org/10.1038/308832a0

Capaccioni F, Cerroni P, Coradini M, Martino MD et al (1986) Asteroidal catastrophic collisions simulated by hypervelocity impact experiments. Icarus 66:487–514. https://doi.org/10.1016/0019-1035(86)90087-4

Delbo M, Libourel G, Wilkerson J, Murdoch N, Michel P, Ramesh KT, Ganino C, Verati C, Marchi S (2014) Thermal fatigue as the origin of regolith on small asteroids. Nature 508:233–236. https://doi.org/10.1038/nature13153

Fujiwara A, Kamimoto G, Tsukamoto A (1978) Expected shape distribution of asteroids obtained from laboratory impact experiments. Nature 272:602–603. https://doi.org/10.1038/272602a0

Heiken GH, Vaniman DT, French BM (eds) (1991) Lunar sourcebook. Cambridge University Press, New York

Heywood H (1971) Particle size and shape distribution for lunar fines sample 12057,72. Proc. Lunar Sci. Conf. 2nd, 1989–2001

Ikeda S, Nakano T, Nakashima Y (2000) Three-dimensional study on the interconnection and shape of crystals in a graphic granite by X-ray CT and image analysis. Mineral Mag 64:945–959. https://doi.org/10.1180/002646100549760

Katagiri J, Matsushima T, Yamada Y, Tsuchiyama A, Nakano T, Uesugi K, Ohtake M, Saiki K (2014) Investigation of 3D grain shape characteristics of lunar soil retrieved in apollo 16 using image-based discrete-element modeling. J Aerosp Eng. 10:1061–1073

Lauretta DS, DellaGiustina DN, Bennett CA, Golish DR, Becker KJ et al (2019) The unexpected surface of asteroid (101955) Bennu. Nature 568:55–60. https://doi.org/10.1038/s41586-019-1033-6

Liu Y, Park J, Schnare D, Hill E, Taylor LA (2008) Characterization of lunar dust for toxicological studies. ii: texture and shape characteristics. J Aerospace Eng 21:272–279

Mahmood A, Mitchell JK, Carrier WD III (1974) Particle shapes of three lunar soil samples. Unpublished report, available from W. D. Carrier III

Matsumoto T, Tsuchiyama A, Uesugi K, Nakano T, Uesugi M, Matsuno J, Nagano T, Shimada A, Takeuchi A, Suzuki Y, Nakamura T, Nakamura M, Gucsik A, Nagaki K, Sakaiya T, Kondo T (2016) Nanomorphology of Itokawa regolith particles: Application to space-weathering processes affecting the Itokawa asteroid. Geochim Cosmochim Acta 187:195–217. https://doi.org/10.1016/j.gca.2016.05.011

Matsushima T, Katagiri J, Uesugi K, Tsuchiyama A, Nakano T (2009) 3D shape characterization and image-based DEM simulation of the Lunar soil simulant FJS-1. J Aerospace Eng 22:15–23. https://doi.org/10.1061/(ASCE)0893-1321(2009)22:1(15)

Michikami T, Hagermann A, Kadokawa T, Yoshida A, Shimada A, Hasegawa S, Tsuchiyama A (2016) Fragment shapes in impact experiments ranging from cratering to catastrophic disruption. Icarus 264:316–330. https://doi.org/10.1016/j.icarus.2015.09.038

Michikami T, Kadokawa T, Tsuchiyama A, Hagermann A, Nakano T, Uesugi K, Hasegawa S (2018) Influence of petrographic textures on the shapes of impact experiment fine fragments measuring several tens of microns: Comparison with Itokawa regolith particles. Icarus 302:109–125. https://doi.org/10.1016/j.icarus.2017.10.040

Molaro LJ, Byrne S, Langer AS (2015) Grain-scale thermoelastic stresses and spatiotemporal temperature gradients on airless bodies, implication for rock breakdown. J Gophys Res Planets 120:255–277. https://doi.org/10.1002/2014JE004729

Morris RV (1977) FMR and magnetic properties of Luna 24 soils and >1 mm particles. Abstr Papers Pres Conf Luna 24:121–124

Tsuchiyama *et al. Earth, Planets and Space*   (2022) 74:172

Page 11 of 11

Morris RV (1978) The surface exposure (maturity) of lunar soils; some concepts and Is/FeO compilation. Proc. Lunar Planet Sci Conf 9th, 2287–2297

Nakamura T, Matsumoto M, Amano K, Enokido Y et al (2022) Formation and evolution of carbonaceous asteroid Ryugu: Direct evidence from returned samples. Science. https://doi.org/10.1126/science.abn8671

Nakano T, Tsuchiyama A, Uesugi K, Uesugi M, Shinohara K (2006) "Slice" –Softwares for basic 3-D analysis-, Slice Home Page (web), http://www-bl20.spring8.or.jp/slice/,Japan Synchrotron Radiation Research Institute (JASRI)

Nakano TN, Y, Nakamura K, Ikeda S, (2000) Observation and analysis of internal structure of rock using X-ray CT. J Geol Soc Japan 106:363–378 (**in Japanese**)

Pieters CM, Noble SK (2016) Space weathering on airless bodies. J Geophys Res Planets 121:1865–1884. https://doi.org/10.1002/2016JE005128

Rode OD, Ivanov AV, Tarasov (1980) Lithology and stratification of the Luna-24 core. In: Lunar soil from Mare Crisium. (A81–32026 13–91) Moscow, Izdatel'stvo Nauka, pp 51–57. In Russian

Stakheev Iul (1979) Characteristics of particle size distributions of lunar soil. In: Lunar highland soil (A80–14621 03–91) Moskow, Izdatel'stvo Nauka, pp77–82. In Russian

Tachibana S, Sawada H, Okazaki R, Takano Y et al (2022) Pebbles and sand on asteroid (162173) Ryugu: In situ observation and particles returned to Earth. Science 375:1011–1016. https://doi.org/10.1126/science.abj8624

Tsuchiyama A, Uesugi M, Matsushima T, Michikami T, Kadono T, Nakamura T, Uesugi K, Nakano T, Sandford SA, Noguchi R, Matsumoto T, Matsuno J, Nagano T, Imai Y, Takeuchi A, Suzuki Y, Ogami T, Katagiri J, Ebihara M, Ireland TR, Kitajima F, Nagao K, Naraoka H, Noguchi T, Okazaki R, Yurimoto H, Zolensky ME, Mukai T, Abe M, Yada T, Fujimura A, Yoshikawa M, Kawaguchi J (2011) Three-Dimensional Structure of Hayabusa Samples: Origin and Evolution of Itokawa Regolith. Science 333:1125–1128. https://doi.org/10.1126/science.1207807

Tsuchiyama A, Uesugi M, Uesugi K, Nakano T, Noguchi R, Matsumoto T, Matsuno J, Nagano T, Imai Y, Shimada A, Takeuchi A, Suzuki Y, Nakamura T, Noguchi T, Abe M, Yada T, Fujimura A (2014) Three-dimensional microstructure of samples recovered from asteroid 25143 Itokawa: comparison with LL5 and LL6 chondrite particles. Meteorit Planet Sci 49:172–187. https://doi.org/10.1111/maps.12177

Tsuchiyama A, Sakurama T, Kadoka T, Ogawa M, Michikami T (2017) Shape evolution of regolith particles on airless bodies; comparison with returned samples and impact and abrasion experiments. Abstract in JpGU, PPS03–13

Usui T, Bajo-Ki-Fujiya W, Furukawa Y, Koike M, Miura YN, Sugahara H, Tachibana S, Takano Y (2020) The Importance of phobos sample return for understanding the mars-moon system. Space Sci Rev 216:49. https://doi.org/10.1007/s11214-020-00668-9

Publisher's Note

Springer Nature remains neutral with regard to jurisdictional claims in published maps and institutional affiliations.